# Waste Heat to Power: Full-Cycle Analysis of a Thermally **Regenerative Flow Battery**

Mirko Engelpracht,\* Markus Kohrn, Dominik Tillmanns, Jan Seiler, and André Bardow\*

Large amounts of waste heat, below 120 °C, are released globally by industry. To convert this low-temperature waste heat to power, thermally regenerative flow batteries (TRFBs) have recently been studied. Most analyses focus on either the discharging or the regeneration phase. However, both phases have to be considered to holistically assess the performance of the flow battery. Therefore, a dynamic, open-access, full-cycle model of a Cu-NH<sub>3</sub> TRFB is developed in Modelica and validated with data from the literature. Based on the validated model, a trade-off between power density and efficiency is shown that depends only on the discharging strategy of the flow battery. For a sensible heat source with an inlet temperature of 120 °C and heat transfer at a thermodynamic mean temperature of about 90 °C, the power density reaches 38 W m<sup>-2</sup> over a complete cycle, and the efficiency reaches 20% of Carnot efficiency. In a benchmarking study, the power production of the flow battery is shown to already achieve 34% of a fully optimized organic Rankine cycle. Thus, TRFBs require further optimization to become a competitive technology for power production and energy storage from low-temperature waste heat.

# 1. Introduction

To achieve the climate goals of the Paris Agreement, efficient use of energy is critical. Still, approximately 30% (31.9 EJ) of the energy input to global industry is lost as waste heat, with 28% as so-called low-temperature waste heat between 60 and 120 °C.[1] Therefore, using low-temperature waste heat offers an opportunity to develop the potential of waste heat and thereby reduce global greenhouse gas emissions.

Technologies to utilize low-temperature waste heat can be divided into three categories: 1) passive heat recovery (e.g., heat exchangers); 2) heat transformation (e.g., heat pumps); and

3) power production (e.g., organic Rankine cycles (ORCs)).[2] Among these technologies, power-production technologies have the advantage that electrical power has a higher energy quality than heat. Thus, power production from lowtemperature waste heat is a promising

For power production from low-temperature waste heat, the ORC can be considered as state-of-the-art technology.<sup>[3]</sup> The advantages of ORCs include the use of standard components, often known from the well-researched Rankine cycle, and the possibility of using working fluids perfectly tailored for a specific application.<sup>[4]</sup> Despite the advantages, today's ORCs are often unprofitable for converting low-temperature heat due to their system complexity and low thermal efficiencies. [4,5]

Rahimi et al.<sup>[6]</sup> have recently reviewed three alternative technologies for power

production from low-temperature waste heat: 1) thermo-osmotic energy conversion (TOEC); 2) thermally regenerative electrochemical cycle (TREC); and 3) thermally regenerative battery

TOEC are turbine-based systems that exploit a static pressure difference between a high-pressure reservoir at ambient temperature and a low-pressure reservoir at heat source temperature.<sup>[6]</sup> TOEC directly integrates heat by vaporizing water through a vapor-permeable membrane from the low-pressure to the high-pressure reservoir.<sup>[7]</sup>

The TREC is an electrochemical cell that exploits a temperaturedependent redox couple. [6] The temperature dependence allows

M. Engelpracht, D. Tillmanns Technical Thermodynamics Faculty of Mechanical Engineering RWTH Aachen University 52062 Aachen, Germany E-mail: mirko.engelpracht@ltt.rwth-aachen.de

The ORCID identification number(s) for the author(s) of this article can be found under https://doi.org/10.1002/ente.202200152.

© 2022 The Authors. Energy Technology published by Wiley-VCH GmbH. This is an open access article under the terms of the Creative Commons Attribution-NonCommercial License, which permits use, distribution and reproduction in any medium, provided the original work is properly cited and is not used for commercial purposes.

DOI: 10.1002/ente.202200152

M. Kohrn Thermodynamics of Mobile Energy Conversion Systems Faculty of Mechanical Engineering **RWTH Aachen University** 52074 Aachen, Germany

J. Seiler, A. Bardow

Energy & Process Systems Engineering Department of Mechanical and Process Engineering ETH Zurich

8092 Zürich, Switzerland E-mail: abardow@ethz.ch

#### A. Bardow

Institute of Energy and Climate Research - Energy Systems Engineering (IEK-10)

Forschungszentrum Jülich GmbH 52425 Jülich, Germany

2194926, 2022, 8, Dowloaded from https://onlinelibrary.wiley.com/doi/10.1002/ente.202200152 by Forschungszentrum Hilch GmbH Research Center, Wiley Online Library on [13/11 2022]. See the Terms and Conditions (https://onlinelibrary.wiley.com/terms-and-conditions) on Wiley Online Library for rules of use; OA articles are governed by the applicable Creative Commons Licenses.

discharging of the electrochemical cell with a high voltage at ambient temperature and charging of the electrochemical cell with a low voltage at higher temperatures.<sup>[7]</sup> Thus, TRECs directly integrate heat to allow heating of the electrochemical cell for charging.

The TRB is an electrochemical cell that uses two almost identical half cells with the only difference being that the anolyte contains an additional ligand. [6] The ligand causes a difference in chemical potential between the half cells, allowing the TRB to produce power. [7] TRBs indirectly integrate heat when distilling off the ligand from the anolyte.

To characterize these three technologies, Rahimi et al. use the relative efficiency  $\eta_{\text{th/Carnot}}$  and power density p (Figure 1). [6] The relative efficiency is the ratio of the thermal efficiency  $\eta_{\text{th}}$  to the Carnot efficiency  $\eta_{\text{Carnot}}$ , and the power density is the ratio of the net electrical power  $P_{\text{el}}$  to the projected surface area of the membrane  $A_{\text{membrane}}$  or electrode  $A_{\text{electrode}}$ .

When comparing the three technologies, TRBs are particularly promising due to high power densities while also achieving high relative efficiencies. A high-power density favorably correlates with system size and, thus, with investment costs. [18] Therefore, we focus on TRBs in this work.

TRBs have primarily been analyzed experimentally, focusing on the discharging phase. For the first time, Peljo et al. have demonstrated the experimental feasibility of thermal regeneration of an all-copper redox flow battery by adding acetonitrile as the ligand. [19] Since then, TRBs have been frequently studied to improve their power densities, efficiencies, long-term stabilities, or cell voltages. Various studies show that power density and efficiency can be increased when using anion-exchange membranes with low resistances,  $^{[12]}$  replacing the ligand with ammonia  $^{[8]}$  or ethylenediamine,  $^{[11]}$  or optimizing the electrolyte compositions and temperatures.<sup>[9]</sup> In particular, the further development of the Cu-NH3 TRB toward a Cu-NH3 thermally regenerative flow battery (TRFB) reduces its system size while increasing its efficiency and power density. [10] The long-term stability of TRB and TRFB were shown to increase by either using silver-based electrodes<sup>[13]</sup> or by additional ligands to prevent deposition and dissolution reactions. [20] Cell voltages were increased by developing, for example, a Cu-MeCn thermally regenerative nanoslurry flow

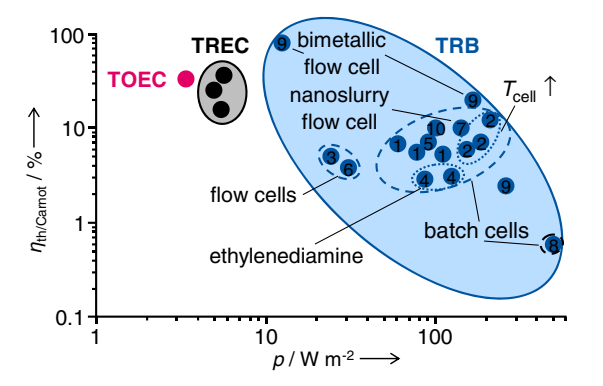


**Figure 1.** Relative efficiency  $\eta_{\text{th/Carnot}}$  and power density p for following technologies (redrawn and extended from Rahimi et al. <sup>[6]</sup>): 1) TOEC—thermo-osmotic energy conversion; 2) TREC—thermally regenerative electrochemical cycle; and 3) TRB—thermally regenerative battery. For TRBs, the figure distinguishes different research topics. Data is taken from 1, <sup>[8]</sup> 2, <sup>[9]</sup> 3, <sup>[10]</sup> 4, <sup>[11]</sup> 5, <sup>[12]</sup> 6, <sup>[13]</sup> 7, <sup>[14]</sup> 8, <sup>[15]</sup> 9, <sup>[16]</sup> 10, <sup>[17]</sup>

battery with propylene as co-solvent  $^{[14]}$  or a bimetallic Cu–Zn–NH $_3$  TRB. $^{[15]}$ 

To further improve TRFBs and decrease experimental costs, Wang et al. developed numerical TRFB models.  $^{[16,21]}$  Based on their validated model for the discharging phase of a Cu–NH $_3$  TRFB,  $^{[21]}$  Wang et al. developed a full-cycle model of a Cu–Zn–NH $_3$  TRFB.  $^{[16]}$  They validated the discharging phase with experimental data, demonstrating excellent agreement.  $^{[16]}$  Moreover, they found that the highest power density leads to the lowest relative efficiency and vice versa.  $^{[16]}$ 

Tian et al. have further developed the model for the discharging phase of the Cu–NH<sub>3</sub> TRFB to optimize the electrolyte flow channels.<sup>[22]</sup> Thereby, they found three design rules to maximize the power density.<sup>[22]</sup> Cross et al. have been studied a 2D model of an Ag–NH<sub>3</sub> TRFB to design a porous electrode with variable void fractions to simultaneously slow clogging and increase the flow battery's power density.<sup>[23]</sup>

Several studies have also experimentally demonstrated the positive effects of optimized electrodes on the power density of Cu–NH<sub>3</sub> TRB and Cu–NH<sub>3</sub> TRFB, respectively. For example, increases in power density were found when using copper foam electrodes,<sup>[24]</sup> porous copper foam electrodes without additional electrolyte flow channels,<sup>[25]</sup> porous copper foam electrodes with decreasing void fraction along the electrolyte flow direction,<sup>[26]</sup> 3D-printed porous carbon electrodes electroplated with copper,<sup>[27]</sup> or porous bimetallic copper foam electrodes.<sup>[17]</sup>

While most authors focus on the discharging phase, Vicari et al.  $^{[28]}$  have studied various regeneration approaches for a Cu–NH $_3$  TRB based on distillation processes. They found that regeneration temperatures around 90 °C at atmospheric pressure are necessary to separate ammonia from the anolyte since ammonia mainly exists as a complex molecule and not as a free molecule.  $^{[28]}$ 

However, for a comprehensive assessment of power density and efficiency, it is necessary to consider the whole process of the TRFB, including the discharging and regeneration phase. The pioneering study of the entire battery cycle by Wang et al. [16] establishes the fundamentals but does not analyze the discharge strategy in detail. Such an analysis is needed to systematically evaluating the trade-off between power density and efficiency during dynamic operation. Therefore, in this work, we develop a dynamic model of a Cu-NH3 TRFB that includes the discharging and regeneration phase, and we validate the developed model with experimental data taken from the literature (Section 2). Subsequently, we systematically investigate the trade-off between power density and efficiency by developing and applying a discharge strategy. As a benchmark, we compare the TRFB's performance to an ORC (Section 3). Finally, we present the main conclusions of this work (Section 4).

# 2. Model of the TRFB

We consider a basic TRFB which will be referenced as "flow battery" in the study. The flow battery consists of the following components: two reservoirs to store the catholyte and anolyte, respectively; two pumps to circulate both electrolytes; an electrochemical cell connected to an electrical load; and a distillation

21944296, 2022, 8, Downloaded from https://onlinelibrary.wiley.

Jülich GmbH Research Center, Wiley Online Library on [13/11/2022]. See the Terms

nditions) on Wiley Online Library for rules of use; OA articles are governed by the applicable Creative Commons I

www.advancedsciencenews.com

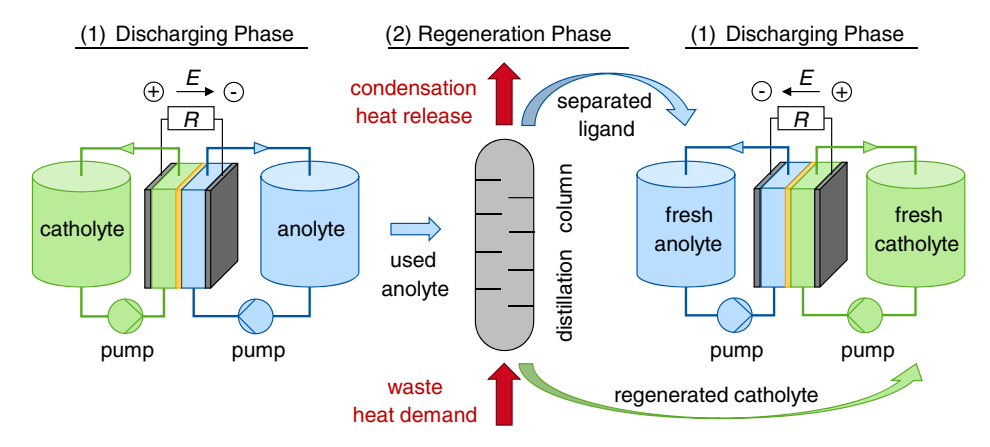


Figure 2. Schematic representation of a thermally regenerative flow battery (TRFB) showing 1) discharging and 2) regeneration phases.

column (**Figure 2**).<sup>[10]</sup> The reservoirs and pumps are components of the periphery, whereas the electrochemical cell and the distillation column are core components of the flow battery. The electrochemical cell is required for the discharging phase of the flow battery and consists of the following three subcomponents<sup>[8]</sup>:

1) two identical electrodes; 2) an anion-exchange membrane; and 3) two electrolytes used as catholyte and anolyte. Both electrolytes are identical except for a ligand (e.g., ammonia) added to the anolyte as an additional component. The distillation column is required for the regeneration phase of the flow battery and separates the ligand from the anolyte.

As shown in Figure 2, the flow battery is an intermitted process that consists of a discharging and a regeneration phase. During the discharging phase, the electrochemical cell electrodes are electrically connected via an electrical load *R*. The potential difference *E* between both electrodes induces a redox reaction that proceeds until reaching electrochemical equilibrium.

During the regeneration phase, a distillation column distills off the ligand from the anolyte. The bottom product of the distillation column is the fresh catholyte in the subsequent discharging phase, while the overhead product of the distillation column is the separated ligand. In the subsequent discharging phase, the separated ligand is added to the old catholyte to become the new anolyte.

In this work, we investigate a Cu–NH<sub>3</sub> flow battery, which has been extensively studied experimentally, based on the results reported in the literature. Thus, the model can be parametrized. At the cathode, copper cations  $Cu_{(aq)}^{2+}$  reduce to copper  $Cu_{(s)}$  by taking up electrons (Equation (1)). At the anode, copper  $Cu_{(s)}$  reacts with ammonia  $NH_{3(aq)}$ , oxidizes to tetraamminecopper (II)  $[Cu(NH_3)_4]_{(aq)}^{2+}$ , and releases electrons (Equation (2)). Thus, the overall redox reaction (Equation (3)) generates a standard cell potential  $E_{cell}^0$  of 0.38 V when discharging the flow battery. [21]

Cathode: 
$$Cu_{(aq)}^{2+}+2\,e^- \rightarrow Cu_{(s)}$$
 (1)  $E_{crt}^0=+0.34\,\mathrm{V}$ 

Anode: 
$$Cu_{(s)} + 4 NH_{3(aq)} \rightarrow [Cu(NH_3)_4]_{(aq)}^{2+} + 2 e^-$$
  
 $E_{ano}^0 = -0.04V$  (2)

Cell: 
$$Cu_{(aq)}^{2+} + 4 NH_{3(aq)} \rightarrow [Cu(NH_3)_4]_{(aq)}^{2+}$$
  
 $E_{cell}^0 = +0.38V$  (3)

We present modeling approaches used for both phases and their validations in the following subsections.

# 2.1. Model of the Discharging Phase

For the discharging phase, we use the modeling approach developed by Wang et al.[21] for a dynamic model in COMSOL Multiphysics. The COMSOL model is based on an experimental setup from Zhu et al.[10] adapted by Wang et al.[21] Geometric details of the experimental setup, which are required to parametrize the COMSOL model, are included in Section A. Supporting Information. We transfer the COMSOL model of the discharging phase to the object-oriented, acausal, dynamic modeling language Modelica<sup>[29]</sup> (Figure 3) to later link the Modelica model of the discharging phase with the Modelica model of the regeneration phase. Thus, we obtain a single model of the full-cycle flow battery in Modelica, allowing studies to be performed in a single simulation software. Additionally, the Modelica model offers the advantage that it can be easily extended: for example, transient heat sources, heat sinks, and power demands can be quickly specified, or control loops for the fullcycle flow battery can be simply integrated. Both the Modelica model of the full-cycle flow battery developed and its underlying Modelica library are made available open access for further use (cf. Supporting Information).

The discharging phase model (cf. Figure 3a) consists of two pumps, an electrical load, and an electrochemical cell, neglecting the two electrolyte reservoirs (cf. Figure 2). We neglect the electrolyte reservoirs since they only affect the hydraulics and time constant of the system, which is outside the scope of this work. Hence, the electrolytes are recirculated directly from the outlets to the inlets of the electrochemical cell, are ideally mixed, and enter the electrochemical cell as homogenous electrolyte flows. The electrochemical cell model (cf. Figure 3b) is 2D discretized to resolve transport effects caused by electrolyte flows along the electrode surfaces and diffusion and electrical migration between the electrodes. According to a laminar flow pattern, the

www.advancedsciencenews.com

www.entechnol.de

21944296, 2022, 8, Downloaded from

Wiley Online Library on [13/11/2022]. See the Terms

rules of use; OA articles are governed by the applicable Creative Commons

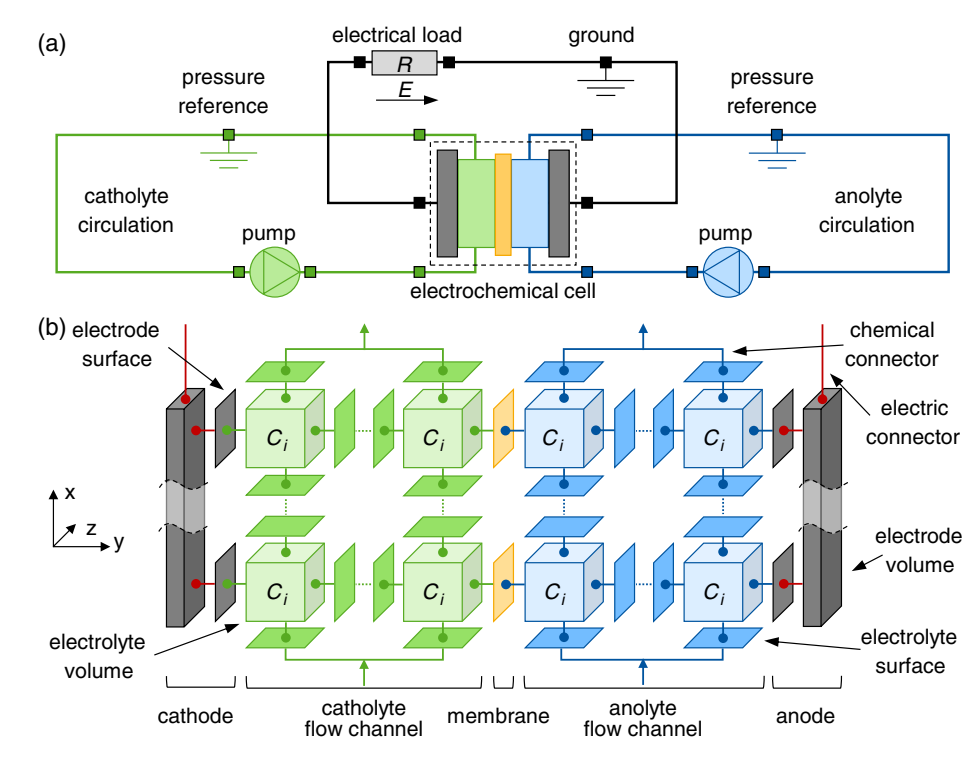


Figure 3. Scheme of the Modelica model of the discharging phase of a Cu–NH<sub>3</sub> TRFB based on a model developed by Wang et al.<sup>[21]</sup>: a) overview of the whole model and b) details of the model of the electrochemical cell, having 2D discretized electrolyte volumes with concentrations  $C_i$  of the species i as differential states.

electrolyte flows have constant velocities depending on the y-coordinate. Overall, the model consists of the following five sub-models: 1) electrode volumes; 2) electrode surfaces; 3) electrolyte volumes; 4) electrolyte surfaces; and 5) membranes. The two volumes are implemented as finite volumes, and the 2D discretization is realized using an upwind finite-difference scheme. Finally, aggregating the five sub-models, as shown in Figure 3b, yields the electrochemical cell model.

Using the models listed before, the averaged power density over one cycle  $\overline{p}$  and averaged current density over one cycle  $\overline{i}$  are given by

$$\overline{p} = \frac{1}{t_{\text{cycle}}} \int_{t=0}^{t_{\text{cycle}}} p dt = \frac{1}{t_{\text{cycle}}} \int_{t=0}^{t_{\text{cycle}}} \frac{P_{\text{el}}}{A_{\text{electrode}}} dt$$
 (4)

$$\bar{i} = \frac{1}{t_{\text{cycle}}} \int_{t=0}^{t_{\text{cycle}}} i dt = \frac{1}{t_{\text{cycle}}} \int_{t=0}^{t_{\text{cycle}}} \frac{I}{A_{\text{electrode}}} dt$$
 (5)

where  $t_{\rm cycle}$  is the time of one discharging phase, p is the electrical power density, i is the current density,  $P_{\rm el}$  is the electrical power, I is the electrical current, and  $A_{\rm electrode}$  is the projected surface area of one electrode (8 cm² is used in this study). Both the averaged power density  $\overline{p}$  and averaged current density  $\overline{i}$  are often used to compare different flow batteries in the literature.  $[^{[21]}]$ 

The electrical power  $P_{\rm el}$  is given by

$$P_{\rm el} = E_{\rm cell} I \tag{6}$$

where  $E_{\rm cell}$  describes the cell voltage. The cell voltage  $E_{\rm cell}$  is the difference of electric potentials between the cathode  $\Phi_{\rm sur,cat}$  and the anode  $\Phi_{\rm sur,ano}$ 

$$E_{\text{cell}} = \phi_{\text{sur.cat}} - \phi_{\text{sur.ano}} \tag{7}$$

where  $\Phi_{\rm sur,ano}$  is fixed at 0 V.<sup>[21]</sup> Similarly to fuel cells,<sup>[30]</sup> both electrodes are modeled as equipotential surfaces since the electrical conductivity of the electrodes is much higher than the electrical conductivity of the electrolytes. Hence, changes in the electric potentials along the electrodes can be neglected.

The electrical current I depends on the reaction kinetics of the redox reaction and is calculated using the Butler–Volmer expression<sup>[31]</sup>

$$I = I_{\text{exchange}} \left[ \exp \left( \frac{\alpha z_{\text{charge}} F}{RT^0} \zeta^{\text{activation}} \right) - \exp \left( -\frac{(1 - \alpha) z_{\text{charge}} F}{RT^0} \zeta^{\text{activation}} \right) \right]$$
(8)

where  $I_{\rm exchange}$  describes the exchange current,  $\zeta^{\rm activation}$  is the activation overpotential,  $\alpha$  is the charge-transfer coefficient,  $z_{\rm charge}$  is the charge number, F is the Faraday constant, R is the ideal gas constant, and  $T^0$  is the temperature at standard conditions (i.e., 298.15 K). The exchange current  $I_{\rm exchange}$  describes the electrical current on the surface of an electrode at electrochemical equilibrium<sup>[31]</sup>

21944296, 2022, 8, Downloaded from https://onlinelibrary.wiley.

Jülich GmbH Research Center, Wiley Online Library on [13/11/2022]. See the Terms and Conditions (https://onlinelibrary.wiley.com/term

and-conditions) on Wiley Online Library for rules of use; OA articles are governed by the applicable Creative Commons License

$$I_{\rm exchange} = z_{\rm charge} Fk A_{\rm electrode} (|\nu_{\rm red,i}| C_{\rm ox,i}^{|\nu_{\rm ox,i}|})^{\alpha} (|\nu_{\rm ox,i}| C_{\rm red,i}^{|\nu_{\rm red,i}|})^{1-\alpha} \tag{9}$$

where k describes the reaction rate constant,  $\nu_i$  is the stoichiometric coefficient of species i involved during reduction (red) and oxidation (ox), and  $C_i$  is the concentration of species i.

The activation overpotential  $\zeta^{activation}$  describes the electric potential required to transfer species across the electric field generated around an electrode when an electric current is present.<sup>[32]</sup> The activation overpotential is given by

$$\zeta^{\text{activation}} = \phi_{\text{sur}} - \phi_{\text{electrolyte}} - E^{\text{Nernst}}$$
(10)

where  $\Phi_{ ext{sur}}$  describes the electric potential on the surface of the electrode,  $\Phi_{
m electrolyte}$  is the electric potential in the electrolyte, and E<sup>Nernst</sup> is the Nernst potential. The Nernst potential corrects the standard electrode potential  $E^0$  for electrolyte conditions that differ from standard conditions and is calculated by the Nernst equation assuming an ideal solution[33,34]

$$E^{\text{Nernst}}(C) = -\frac{\Delta G_{\text{reaction}}^{0}}{z_{\text{charge}}F} - \frac{RT^{0}}{z_{\text{charge}}F} \ln(\prod_{i} a_{i}^{\nu_{i}})$$

$$\approx -\frac{\Delta G_{\text{reaction}}^{0}}{z_{\text{charge}}F} - \frac{RT^{0}}{z_{\text{charge}}F} \ln\left(\frac{\prod_{i} C_{\text{red},i}^{|\nu_{\text{red},i}|}}{\prod_{i} C_{\text{ox},i}^{|\nu_{\text{ox},i}|}}\right)$$
(11)

where  $\Delta G_{\text{reaction}}^0$  is the Gibbs free energy of the reaction at standard conditions, and  $a_i$  is the activity of species i.

For linking the electrical current to the species involved in the redox reaction on the surface of an electrode, Faraday's law of electrolysis is used<sup>[34]</sup>

$$\frac{\partial n_i}{\partial t} = \frac{I}{z_0 F} \tag{12}$$

where t is the time, and  $n_i$  is the amount of substance of species ithat is converted by the redox reaction. Within the electrolyte, the species *i* is transported by the three mechanisms: 1) diffusion; 2) electrical migration; and 3) convection.<sup>[34]</sup>

$$\frac{\partial n_{i}}{\partial t} = \underbrace{-D_{i}A_{\text{electrode}}\frac{\text{d}C_{i}}{\text{d}y}}_{\text{(i) diffusion}} \underbrace{-D_{i}C_{i}A_{\text{electrode}}\frac{z_{\text{charge},i}F}{RT^{0}}\frac{\text{d}\phi}{\text{d}y}}_{\text{(iii) electrical migration}} \underbrace{+C_{i}A_{\text{electrode}}u_{x}}_{\text{(iii) convection}}$$

Here,  $D_i$  is the diffusion coefficient of species i,  $\Phi$  is the electrical potential,  $u_x$  is the electrolyte velocity in the flow direction, x is the coordinate in the flow direction, and y is the coordinate perpendicular to the surfaces of the electrodes. The first term describes the diffusion perpendicular to the surfaces of the electrodes, the second term describes the electrical migration perpendicular to the surfaces of the electrodes, and the third term describes the convection in the flow direction.

The species transport across the membrane is calculated using Faraday's law of electrolysis (cf. Equation (12)), where the electrical current in the membrane is calculated following a charge balance and Ohm's law.[21]

With the equations presented before and the finite-volume discretization shown in Figure 3b, the COMSOL model of the discharging phase developed by Wang et al.[21] is completely

Table 1. Kinetic and fluid property parameters for the Modelica model of the discharging phase. For more details on the parameter determination, the reader is referred to Wang et al.[21]

Parameter/species	Symbol	Unit	Cathode	Anode	Reference
Electrodes					
Standard potential	E <sup>o</sup>	٧	0.34	-0.04	[35]
Reaction rate constant	k	${\rm m}{\rm s}^{-1}$	$5 \times 10^{-6}$	$7 \times 10^{-7}$	[21]
Electron transfer coefficient	α	_	0.64	0.5	[21]
Charge number	Z <sub>charge</sub>	-	2	2	[35]
Electrolytes					
Gravimetric density	$\rho$	${\rm kg}{\rm m}^{-3}$	1119	1059	[21]
Kinematic viscosity	μ	$\rm m^2s^{-1}$	$0.847\times10^{-6}$	$0.943\times10^{-6}$	[21]
Diffusion coefficients	of species	within e	lectrolytes		
$Cu_{(aq)}^{2+}$	D	$\rm m^2s^{-1}$	$\rm 1.5\times10^{-9}$	_	[21]
$NH_{3(aq)}$	D	$\rm m^2s^{-1}$	-	$0.6\times10^{-9}$	[35]
$[Cu(NH_3)_4]^{2+}_{(aq)}$	D	$\rm m^2s^{-1}$	-	$1.7\times10^{-9}$	[21]
$NO_{3(aq)}^{-} \\$	D	$\rm m^2s^{-1}$	$0.95\times10^{-9}$	$0.95\times10^{-9}$	[35]
$NH_{4(aq)}^+$	D	$\rm m^2s^{-1}$	$0.9\times10^{-9}$	$0.95\times10^{-9}$	[35]

transferred to a Modelica model. Table 1 summarizes the parameters required to parametrize the Modelica model. The whole equation set of the Modelica model is presented in Section A, Supporting Information, while the exact implementation of the equation set into Modelica can be found in the open-access Modelica model itself (cf. Supporting Information).

## 2.2. Model of the Regeneration Phase

The regeneration phase has two objectives: 1) the ligand should be separated entirely from the analyte. [9] The entire separation of the ligand maximizes the ammonia concentration gradient between the two half cells of the electrochemical cell. A reduced ammonia concentration gradient would reduce the potential difference between the two half cells and, thus, the flow battery's power production. A distillation column is suitable to separate the ligand from the analyte using only low-temperature waste heat as driving energy and, consequently, investigated in this work.<sup>[28]</sup>

Simultaneously, the regeneration phase has a second objective: 2) the separated ligand (i.e., the overhead product of the distillation column) should have high purity. The high purity of the ligand avoids a dilution of the new analyte. Dilution of the new anolyte would also reduce the ammonia concentration gradient between the two half cells and, thus, the flow battery's power production.

To model the distillation process, we base our analysis on work by Zhang et al., [8] who 1) assumed that the complex  $[Cu(NH_3)_4]^{2+}_{(aq)}$  mostly dissociates to a copper cation  $Cu^{2+}_{(aq)}$ and ammonia NH<sub>3 (aq)</sub>; and 2) only calculates the thermal energy required for distillation. However, the dissociation reaction rate depends on the distillation temperature[28] and should be

checked for the chosen temperatures in future work. The dissociation reaction is given by

$$[Cu(NH_3)_4]_{(aq)}^{2+} \rightarrow Cu_{(aq)}^{2+} + 4NH_{3(g)} \tag{14} \label{eq:14}$$

Therefore, we model the feed stream of the distillation column, which is the analyte of the previous discharging phase, as a binary mixture that consists only of water and ammonia.

Apart from this assumption on the feed stream, the distillation process design mainly depends on the temperatures of the reboiler and condenser. For example, a single distillation column operating at atmospheric pressure (Figure 4) fulfills the regeneration phase objectives when using a heat source above 100 °C and a heat sink below 20 °C. However, when reducing the heat source temperature below 100 °C, the same distillation column violates the purity requirements due to the boiling point of nearly pure water in the reboiler. Therefore, for fulfilling the purity requirements for heat sources below 100 °C, a more complex distillation process is necessary, such as a pressure-swing distillation process (cf. Figure B1, Supporting Information). To analyze the impacts of different heat source temperatures on the flow battery's performance, we exemplarily investigate 1) a simple distillation process using a sensible heat source with an inlet temperature of 120 °C and heat transfer at a thermodynamic mean temperature of approximately 90 °C; and 2) a more complex distillation process using a sensible heat source with an inlet temperature of 85 °C and heat transfer at a thermodynamic mean temperature of approximately 70 °C. Heat sources with other inlet temperatures are also possible but may require adjustment of the distillation process design. The feasibility of regeneration temperatures up to 100 °C has been experimentally

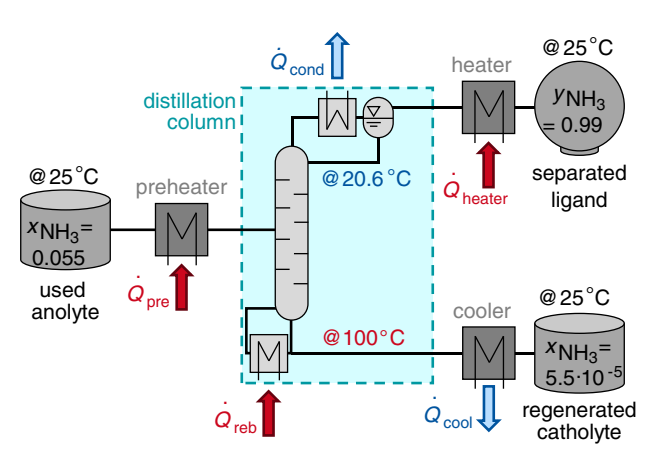


Figure 4. Scheme of a simple regeneration process using a sensible heat source with an inlet temperature of 120 °C and heat transfer at a thermodynamic mean temperature of approximately 90 °C, a heat sink at 15 °C, and a distillation column at atmospheric pressure. The feed stream is a liquid water-ammonia mixture at 25 °C with a constant liquid ammonia mole fraction  $x_{\rm NH_3}$  of 5.5 mol%. The overhead product is a vapor stream with a vapor ammonia mole fraction  $y_{\text{NH}_3}$  of 99.0 mol%, and the bottom product is a liquid stream with a liquid ammonia mole fraction  $x_{NH_2}$  of  $5.5 \times 10^{-5}$  mol%. Heat inputs are the heat flows of the preheater  $\dot{Q}_{\rm pre}$ , reboiler  $\dot{Q}_{\text{reb}}$ , and heater  $\dot{Q}_{\text{heater}}$ ; heat outputs are the heat flows of the condenser  $\dot{Q}_{con}$  and cooler  $\dot{Q}_{cool}$ .

demonstrated by Vicari et al., [28] while previous studies on flow batteries, for example, studies conducted by Zhang et al., [9] often assume lower regeneration temperatures of around 70 °C.

We develop steady-state process models using Aspen Plus, commonly used for process modeling and simulation, for designing both distillation processes.[36] Required fluid properties of the binary mixture of water and ammonia are also calculated using Aspen Plus<sup>[36]</sup> based on RefProp<sup>[37]</sup> with the equation of state from Tillner-Roth and Friend. [38] To maximize the yields of the distillation processes for a given mass flow of a sensible heat source (e.g., liquid industrial wastewater), we indirectly minimize the mass flow of the heat source  $\dot{m}_{\rm source}$  required to regenerate a feed stream of 1 L s<sup>-1</sup> by minimizing the heat flow of the reboiler  $Q_{reb}$ . When minimizing the heat flow of the reboiler, the mass flow of the sensible heat source is also minimized due to a minimum pinch temperature at the outlet of the reboiler. Thus, for example, the optimization problem of the simple regeneration process reads as follows

$$\begin{array}{ll} \underset{N_{\mathrm{Stage}},\ N_{\mathrm{pre}},\ RR,\ DF}{\min} & \dot{Q}_{\mathrm{reb}}(z,\Theta) \ \ (\mathrm{objective\,function}) \\ & s.t. & 0 = g(z,\Theta) \ \ (\mathrm{steady\text{-}state\,process\,model}) \\ & \gamma_{\mathrm{NH}_3} \geq 0.99 \ \ (\mathrm{purity\,and\,temperature\,constraints}) \\ & \varkappa_{\mathrm{NH}_3} \leq 5.5 \times 10^{-5} \\ & T_{\mathrm{pinch}} \geq 2\mathrm{K} \\ & 0 \leq N_{\mathrm{stage}} \leq 20 \ \ (\mathrm{degrees\,of\,freedom}) \\ & 0 \leq N_{\mathrm{pre}} \leq N_{\mathrm{stage}} \\ & 0 \leq RR \leq \infty \\ & 0 \leq DF \leq 1 \end{array}$$

where z describes the algebraic states and  $\Theta$  are the timeinvariant parameters.

The optimization problem is solved subjected to (s.t.) the steady-state process model of the distillation process, described by an algebraic equation system. For ensuring the required purities of the products, constraints are added for the vapor mole fraction of the overhead product  $\gamma_{NH_3}$  and the liquid mole fraction of the bottom product  $x_{NH_2}$ . Additionally, a minimal pinch temperature  $T_{\text{pinch}}$  of 2 K is applied for all heat exchangers. The objective function is minimized by optimizing the following four design parameters of the distillation process: 1) number of equilibrium stages  $N_{\text{stage}}$ ; 2) inlet stage of the feed stream  $N_{\text{pre}}$ ; 3) reflux ratio RR; and 4) ratio of distillate flow rate to feed flow rate DF.

As well as the constraints presented before, we base other specifications of the optimization problem on both the operating conditions of the discharging phase and the objective of recovering low-temperature waste heat. The feed stream operates at 25 °C and 1 bar with a constant liquid ammonia mole fraction of 5.5 mol%, which corresponds to an ammonia concentration of 3 mol L<sup>-1</sup>, and the product streams have a temperature of 25 °C. The ammonia mole fraction is constant since the ammonia is completely dissolved in the constant analyte volume, and very little nitrate diffuses through the membrane. The heat input required to heat the separated gaseous ligand to 25 °C is neglected for further calculations since it is small compared to all other heat inputs (<3.5%). The inlet temperature of the

21944296, 2022, 8, Downloaded from https://onlinelibrary.wiley.com/doi/10.1002/ente.202200152 by Forsch

Jülich GmbH Research Center, Wiley Online Library on [13/11/2022]. See the Terms and Conditions (https://onlinelibrary.wiley.com/terms

and-conditions) on Wiley Online Library for rules of use; OA articles are governed by the applicable Creative Commons I

sensible heat source is 120 °C for the single-stage distillation column and 85 °C for the pressure–swing distillation process, with heat transfer at thermodynamic mean temperatures of approximately 90 and 70 °C, respectively. For both distillation processes, the inlet temperature of the sensible heat sink is 15 °C, and its outlet temperature is restricted to 18 °C. We use water for the sensible heat source and sink, modeled as an ideal liquid with a constant specific heat capacity of  $4.18 \, \mathrm{kJ \, kg^{-1} \, K^{-1}}$ .

To solve the optimization problem, we use the built-in optimization tool of Aspen Plus.  $^{[36]}$  For the single-stage distillation column and a feed flow of  $1\,L\,s^{-1}$ , the split factor of ammonia is 0.9992, the split factor of water is 0.0006, the heat input is 789 kW, the heat output is 620 kW (i.e., 324 kW for the condenser and 296 kW for the cooler), the mass flow of the heat source is  $3.0\,kg\,s^{-1}$ , and the mass flow of the heat sink is 49.4 kg s $^{-1}$ . Thus, the heat source cools from 120 to 58 °C, and the heat sink heats from 15 to 18 °C. Thereby, none of the degrees of freedom reach their lower or upper bounds. The optimization results of the pressure—swing distillation process are provided in Section B, Supporting Information.

To integrate the Aspen Plus optimization results into Modelica, we normalize the optimization results (e.g., heat flows) by the feed flow (i.e.,  $1\,\mathrm{L\,s^{-1}}$ ). Then, we integrate the normalized results into Modelica as a black-box model, allowing us to calculate the required heat flows in Modelica by multiplying the normalized results by the required feed flow. Thus, the results of the Aspen Plus optimization are transferred exactly as is into a black-box model in Modelica.

# 2.3. Validation of the Model of the Discharging Phase

To validate the model of the discharging phase (cf. Section 2.1), we compare the steady-state current-voltage characteristic simulated with the Modelica model to the following characteristics of Wang et al.<sup>[21]</sup>: 1) characteristic calculated with the COMSOL model; and 2) characteristic measured with the experimental setup. For both comparisons, the electrolyte concentrations are identical and given in Table S2, Supporting Information. To assess the simulation results of the Modelica model, we define the relative deviation (RD) as

$$\mathrm{RD}_i = \frac{|E_{\mathrm{cell}}^i - E_{\mathrm{cell}}^{\mathrm{sim}}|}{E_{\mathrm{cell}}^{\mathrm{rev}}} \text{ with } i \in \{\mathrm{COMSOL}, \ \mathrm{exp}\}$$

where  $E_{\rm cell}^i$  describes the steady-state voltage calculated with the COMSOL model (i.e.,  $i = {\rm COMSOL}$ ) or measured during the experiments (i.e.,  $i = {\rm exp}$ ),  $E_{\rm cell}^{\rm sim}$  is the steady-state cell voltage simulated with the Modelica model, and  $E_{\rm cell}^{\rm rev}$  is the reversible cell potential for the investigated electrolyte concentration (here 0.42 V). We normalize the absolute deviation to the reversible cell potential  $E_{\rm cell}^{\rm rev}$  and not to the voltage  $E_{\rm cell}^i$  because the relative deviation would otherwise approach infinity for small values of the voltage  $E_{\rm cell}^i$ .

An accurate discharging phase model needs to correctly predict the steady-state current–voltage characteristic within the flow battery's operating range (**Figure 5**). The operating range is defined as the current density range from  $0 \, \text{A m}^{-2}$  to the current density leading to the maximum power density (here 142 A m $^{-2}$ ).

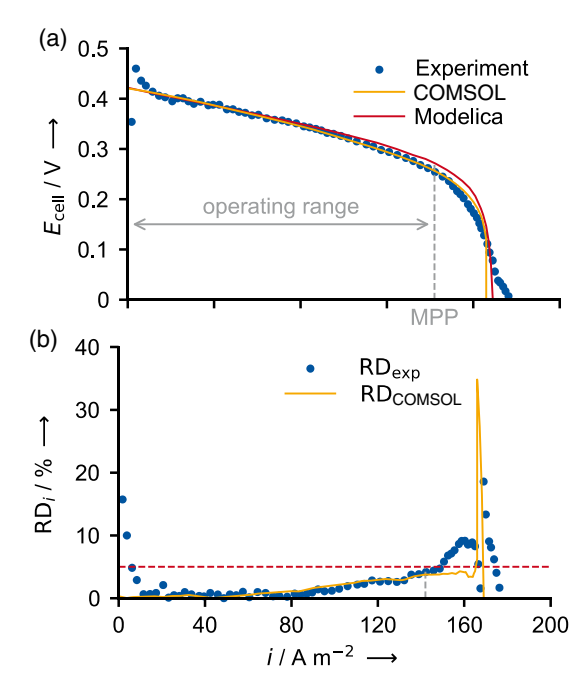


**Figure 5.** Comparison of steady-state cell voltages  $E_{\text{cell}}$  simulated by the Modelica model to voltages calculated with the COMSOL model (i = COMSOL) and voltages measured by Wang et al.  $(i = \exp)$ . [21] a) Cell voltages and b) relative deviations (RD<sub>i</sub>, Equation (16)) are plotted over the current density *i*. The operating range indicates the current density range until reaching the maximum power point (MPP); the dashed red line indicates a relative error limit of 5%.

The maximum power density is reached at the so-called maximum power point (MPP), which is defined similarly to the MPP of fuel cells.<sup>[39]</sup>

The Modelica results show good qualitative and quantitative agreement with the COMSOL results within the operating range of the flow battery (cf. Figure 5): relative deviations RD<sub>COMSOL</sub> are always less than 5% for current densities below 162 A m<sup>-2</sup>. Deviations between the Modelica and COMSOL models may be caused for two reasons. First, due to numerical reasons, we assume fully developed laminar flow profiles for the electrolyte flows calculated using an equidistant discretization grid. In contrast, Wang et al. have calculated the flow profiles using the Laminar Flow toolbox of COMSOL Multiphysics, which uses 3D-geometric models of the electrolyte channels and generates a problem-depending discretization grid automatically. [21] Thus, we simplify the flow profiles of the electrolytes. Moreover, model parameters fitted by Wang et al. may no longer be precisely valid for our flow profiles and discretization grid. Second, we also neglect diffusion in the flow direction for numerical reasons, whereas Wang et al. have considered diffusion in the flow direction. [21] Calculated Peclet numbers of all species range between 1 and 5 near the electrode surfaces, showing that diffusion in the flow direction should not be neglected if numerically feasible. However, although we simplified the Modelica model, the deviations are small between the Modelica and COMSOL models for the flow battery's operating range. Thus, the COMSOL model of the discharging phase is transferred successfully to the Modelica model.

21944296, 2022. 8, Downloaded from https://onlinelibrary.wiley.com/doi/10.1002/ente.202200152 by Forschungszentrum Jülich GmbH Research Center, Wiley Online Library on [13/11/2022]. See the Terms and Conditions (https://onlinelibrary.wiley.com/terms-

and-conditions) on Wiley Online Library for rules of use; OA articles are governed by the applicable Creative Commons Licens

The Modelica results also show good qualitative and quantitative agreement with the experimental results (Figure 5): the average relative deviation (ARD) is 1.33% for the operating range of the flow battery. This accuracy seems excellent, such that the Modelica model should be well suited to model the operating behavior of the flow battery.

Still, it should be noted that the simulation results differ significantly from the experimental data for very-low-current densities lower than 5 A m<sup>-2</sup> and current densities higher than 150 A m<sup>-2</sup>, respectively. In addition, the Modelica model collapses at 162 A m<sup>-2</sup>, which is below the maximum measured current density of 176 A m<sup>-2</sup>. For very-low-current densities, neglecting side reactions may lead to deviations from the experimental data. [21] However, the Modelica model correctly calculates the reversible cell potential. Thus, the deviations at very-lowcurrent densities need to be investigated in more detail in future work. For high-current densities, the deviations may be caused by two effects: 1) neglecting side reactions<sup>[21]</sup>; and 2) using concentration-independent Butler–Volmer expressions, diffusion parameters, and kinetic parameters. [16] In particular, recent models showed that concentration-dependent approaches of the Butler-Volmer expression and the kinetics and diffusion parameters improve the description at very-high-current densities.<sup>[16]</sup> The steady-state current-voltage characteristic simulated by the Modelica model may collapse for lower-current densities than the measured characteristic due to the discussed simplifications and as diffusion in the flow direction is neglected. The diffusion in flow direction is particularly important for high-current densities since high-current densities lead to high reaction rates (cf. Equation (12)) and, thus, to high concentration gradients in the flow direction. Thus, copper cations may deplete at the surface of the cathode in the catholyte flow channel, which causes the simulation to abort immediately.

Nevertheless, larger deviations are significant only at the lower and upper ends of the current density range. In sum, the Modelica model shows good agreement with both the COMSOL model and experimental data for central parts of the flow battery's operating range. Thus, the Modelica model is regarded as sufficiently accurate for the current density range investigated in this work.

## 2.4. Validation of the Model of the Regeneration Phase

When validating the regeneration phase model, the calculated purity of the regenerated electrolytes is crucial (cf. Section 2.2). The purity is calculated by the Aspen Plus model and depends on the steady-state process model and the vaporliquid equilibrium (VLE) data of the binary mixture of water and ammonia. We assume that the steady-state process models of Aspen Plus, often used for process modeling and simulation in literature, are accurate. Therefore, we only compare the VLE data calculated with the Aspen model to experimental VLE data taken from the literature (**Figure 6** and S2, Supporting Information). [40] The uncertainties of calculated mole fractions are always lower than  $\pm 0.01$  for the investigated pressure and temperature range. [38]

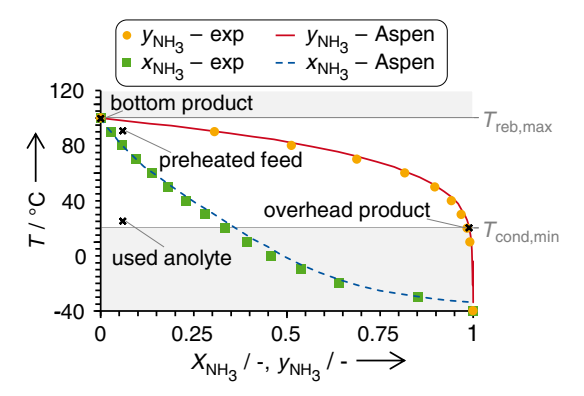


**Figure 6.** Comparison of experimental vapor–liquid equilibrium (VLE) data (exp, dots/squares) of the binary mixture of water and ammonia at 1 bar taken from the literature  $^{[40]}$  with calculated VLE data (Aspen, solid/dashed line) using the equation of state from Tillner-Roth and Friend  $^{[38]}$  implemented in Aspen Plus.  $^{[36]}$  For ammonia,  $x_{\rm NH_3}$  indicates the liquid molar fraction and  $y_{\rm NH_3}$  the vapor molar fraction. The maximal reboiler temperature and the minimal condensing temperature are indicated by  $T_{\rm reb,max}$  or  $T_{\rm cond,min}$  (cf. Section 2.2).

To evaluate the calculated VLE data, we define the ARD as

$$ARD = \frac{1}{N} \sum_{i=1}^{N} \frac{|T_{i}^{exp} - T_{i}^{sim}|}{T_{i}^{exp}}$$
 (17)

where N describes the number of experimental data points (i.e., measured mole fractions),  $T_i^{\rm exp}$  is the corresponding measured temperatures, and  $T_i^{\rm sim}$  are the corresponding temperatures calculated with Aspen Plus. Overall, the calculated VLE data closely agrees with the measured VLE data.

The single-stage distillation process operates at 1 bar. The ARD is 0.93% for the saturated liquid line and 0.79% for the saturated vapor line (Figure 6). As desired for the single-stage distillation process, the ammonia mole fraction is greater than 99 mol% for the overhead product and less than 1 mol‰ for the bottom product when using a maximal reboiler temperature of  $100\,^{\circ}\text{C}$  and a minimal condensing temperature of  $20\,^{\circ}\text{C}$ .

The pressure–swing distillation process additionally operates at 0.275 bar. Here, the ARD is 1.80% for the saturated liquid line and 2.07% for the saturated vapor line (Figure S2, Supporting Information). As desired for the pressure–swing distillation process, the ammonia mole fraction is greater than 99 mol% for the overhead product because the minimal condensing temperature of 20 °C does not change. Moreover, the ammonia mole fraction is less than 1 mol‰ for the bottom product when using a maximal reboiler temperature of 85 °C.

Thus, the ammonia mole fractions, which are required for the products of the regeneration process, can be achieved by both distillation processes investigated in this work.

# 3. Full-Cycle Analysis of a TRFB

In Section 3.1, we show the impacts of operating conditions of the discharging phase on the time trajectories of power density and efficiency. In Section 3.2, we highlight the trade-off between

21944296, 2022, 8, Downloaded from https://onlinelibrary.wiley.com/doi/10.1002/ente.202200152 by Forsch

Jülich GmbH Research Center, Wiley Online Library on [13/11/2022]. See the Terms

and-conditions) on Wiley Online Library for rules of use; OA articles are governed by the applicable Creative Commons

power density and efficiency in detail. Based on these results, we compare the investigated Cu-NH3 flow battery with a fully optimized ORC in Section 3.3.

#### 3.1. Time Trajectories of Power Density and Efficiency

We use the dynamic model of the discharging phase (cf. Section 2.1) and the regeneration phase model that uses a sensible heat source with an inlet temperature of 120 °C (cf. Section 2.2) to analyze the impacts of operating conditions of the discharging phase on the flow battery's performance. We neglect the time required to exchange the electrolytes of the flow battery with the electrolytes regenerated. Moreover, we assume that the gaseous ammonia separated in the regeneration process dissolves entirely in the old catholyte. [41] Using these assumptions, we derive the maximal theoretical potential of the considered flow battery.

As an exemplary operating point, we choose the following conditions: 1) a constant cycle time  $t_{\text{cycle}}$  of 1800 s; 2) a constant electrical load  $R_{\text{TRFB}}$  of 25  $\Omega$ ; 3) an initial copper cation concentration in the catholyte of  $0.4 \, \text{mol L}^{-1}$ ; and 4) an initial ammonia concentration in the analyte of 3 mol L<sup>-1</sup>. For this operating point, we analyze the time trajectories of the power density p, of the relative efficiency  $\eta_{\text{th/Carnot}}$ , of the concentration of copper cations at the inlet of the catholyte  $C_{\text{Cu}^{2+}}^{\text{inlet}}$ , and of the concentration of tetraamminecopper(II) at the inlet of the anolyte  $C_{[Cu(NH_3)_4]^{2+}}^{inlet}$ 

Here, we define the relative efficiency  $\eta_{th/Carnot}$  as the ratio of the thermal efficiency  $\eta_{th}$  and the Carnot efficiency  $\eta_{Carnot}^{[6]}$ 

$$\eta_{\text{th/Carnot}} = \frac{\eta_{\text{th}}}{\eta_{\text{Carnot}}}$$

$$= \frac{E_{\text{cell}}I}{\dot{m}_{\text{source}}c_{\text{source}}(T_{\text{source,inlet}} - T_{\text{source,outlet}})(1 - \frac{T_{\text{low}}}{T_{\text{high}}})}$$
(18)

where  $c_{\text{source}}$  describes the specific heat capacity of the heat source,  $T_{\text{source,inlet}}/T_{\text{source,outlet}}$  is the inlet/outlet temperature of the heat source, and  $T_{\text{high}}/T_{\text{low}}$  is the highest/lowest temperature of the regeneration process. Since our regeneration process does not use isothermal heat sources or sinks, we use thermodynamic mean temperatures of the heat source and heat sink as the highest and lowest temperature of the regeneration process (i.e.,  $T_{\text{source,mean}}$  instead of  $T_{\text{high}}$  and  $T_{\text{sink,mean}}$  instead of  $T_{\text{low}}$ ). The thermodynamic mean temperatures are  $T_{\text{source,mean}}$ = 88.1 °C and  $T_{\text{sink,mean}}$  = 16.5 °C for the single-stage distillation process and  $T_{\text{source},\text{mean}} = 66.2 \,^{\circ}\text{C}$  and  $T_{\text{sink},\text{mean}} = 16.5 \,^{\circ}\text{C}$  for the pressure-swing distillation process. Furthermore, we define the difference between the maximum and minimum concentrations of copper cations at the inlet of the catholyte at cyclic steady-state as the working capacity of copper cations  $\Delta C_{Cu^{2+}}^{\text{inlet}}$ .

The time trajectories highlight the dynamics of the flow battery (Figure 7). The inlet concentrations of copper cations in the catholyte  $C_{Gu^{2+}}^{inlet}$  and of tetraamminecopper(II) in the anolyte  $C_{[Cu(NH_3)_4]^{2+}}^{inlet}$  change continuously due to the ongoing redox reaction (cf. Figure 7c). As a result, the difference in the chemical potential between the cathode and the anode changes, and,

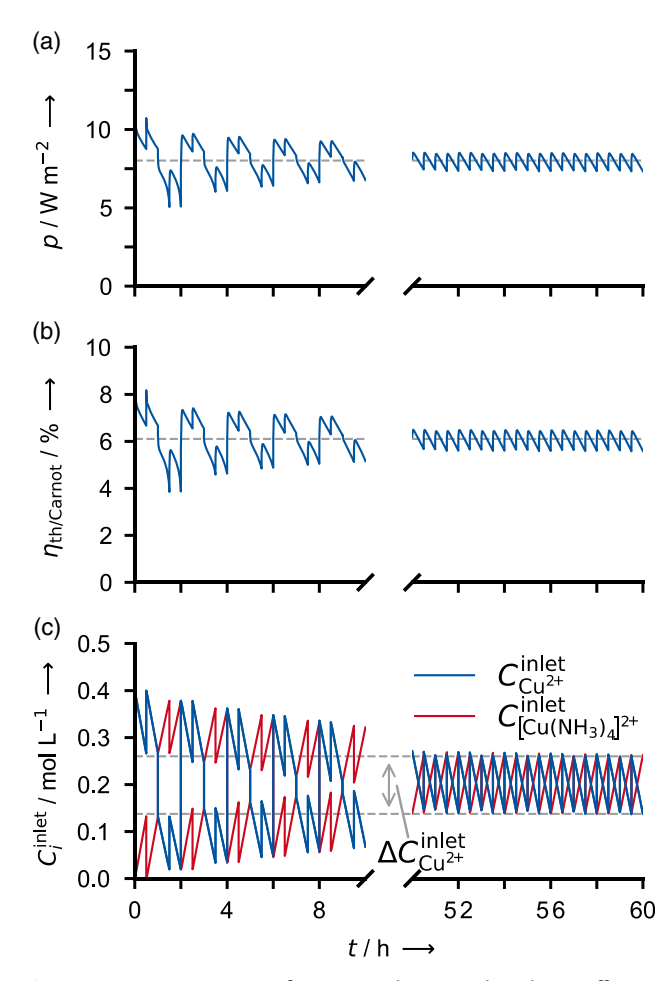


Figure 7. Time trajectories of a) power density p, b) relative efficiency  $\eta_{\text{th/Carnot}}$ , and c) concentration of copper cations at the inlet of the catholyte  $C_{\text{Cu}^{2+}}^{\text{inlet}}$  and of tetraamminecopper(II) at the inlet of the analyte  $C_{[Cu(NH_1)_{\ell}]^{2+}}^{inlet}$  for a constant cycle time ( $t_{cycle} = 1800$  s) and a constant electrical load ( $R_{TRFB} = 25 \Omega$ ). The dashed grey lines indicate time-averaged values in subplots a) and b) and the working capacity of copper cations in subplot c).

consequently, the power density p also changes (cf. Figure 7a). Moreover, Figure 7c shows the flow battery's alternating discharging and regeneration phases. After each discharging phase, the electrolytes are exchanged by electrolytes regenerated simultaneously during the discharging phase. Thus, two "electrolyte sets" exist, starting with the same initial conditions. Consequently, two consecutive discharge phases show the same time trajectories as they always start with the same electrolyte concentrations. The concentrations of the electrolyte sets only change after one full discharge and regeneration cycle.

Additionally, Figure 7 shows the transient response of the flow battery before reaching the cyclic steady state. With increasing time, the power density p fluctuates around  $8.0 \,\mathrm{W}\,\mathrm{m}^{-2}$  (cf. Figure 7a), the relative efficiency  $\eta_{\text{th/Carnot}}$  fluctuates around 6.2% (cf. Figure 7b), and both inlet concentrations  $C_{\mathrm{Cu}^{2+}}^{\mathrm{inlet}}$  and  $C_{[Cu(NH_3)_4]^{2+}}^{inlet}$  fluctuate around 0.2 mol L<sup>-1</sup> (cf. Figure 7c). The inlet concentrations fluctuate around 0.2 mol L<sup>-1</sup> due to the

2194265, 2022, 8, Dowloaded from https://onlinelibrary.wiley.com/doi/10.1002/ente.202200152 by Forschungszentrus Bilded GmbH Research Center, Wiley Online Library on [13/11 2022]. See the Terms and Conditions (https://onlinelibrary.wiley.com/terms-and-conditions) on Wiley Online Library for rules of use; OA articles are governed by the applicable Creative Commons Licensen (13/11 2022). See the Terms and Conditions (https://onlinelibrary.wiley.com/terms-and-conditions) on Wiley Online Library for rules of use; OA articles are governed by the applicable Creative Commons Licensen (13/11 2022). See the Terms and Conditions (https://onlinelibrary.wiley.com/terms-and-conditions) on Wiley Online Library for rules of use; OA articles are governed by the applicable Creative Commons Licensen (13/11 2022). See the Terms and Conditions (https://onlinelibrary.wiley.com/terms-and-conditions) on Wiley Online Library for rules of use; OA articles are governed by the applicable Creative Commons Licensen (13/11 2022). See the Terms and Conditions (https://onlinelibrary.wiley.com/terms-and-conditions) on Wiley Online Library for rules of use; OA articles are governed by the applicable Creative Commons Licensen (13/11 2022). See the Terms and Conditions (https://onlinelibrary.wiley.com/terms-and-conditions) on Wiley Online Library for rules of use; OA articles are governed by the applicable Creative Commons (13/11 2022). See the Terms and Conditions (https://onlinelibrary.wiley.com/terms-and-conditions) on the applicable Creative Commons (13/11 2022). See the Terms and Conditions (https://onlinelibrary.wiley.com/terms-and-conditions) on the applicable Creative Commons (13/11 2022). See the Terms and Conditions (https://onlinelibrary.wiley.com/terms-and-conditions) on the applicable Creative Commons (13/11 2022). See the Terms and Conditions (https://onlinelibrary.wiley.com/terms-and-conditions) on the applicable Creative Commons (13/11 2022). See the Terms and Conditions (https://onlinelibrary.wiley.com/terms-and-conditions) on th

intrinsic dynamics of the flow battery. For each electrolyte set, the initial inlet concentrations are 0.4 and 0.0 mol L<sup>-1</sup> for the copper cations in the catholyte and the tetraamminecopper(II) in the anolyte, respectively (cf. Figure 7c). After the first discharging phase, the inlet concentration of copper cations in the catholyte  $C_{\text{Cu}^{2+}}^{\text{inlet}}$  is close to 0.27 mol L<sup>-1</sup> since not all copper cations are reduced to copper during the discharging phase. The inlet concentration of tetraamminecopper(II) in the anolyte  $C_{\text{inlet}}^{\text{inlet}}$  contraction of the catholyte  $C_{\text{inlet}}^{\text{inlet}}$  contraction of the catholyte of the whole ammonia content from the anolyte to avoid diluting the regene

phase, the inlet concentration of copper cations in the catholyte  $C_{\text{Cu}^{2+}}^{\text{inlet}}$  is close to 0.27 mol L<sup>-1</sup> since not all copper cations are reduced to copper during the discharging phase. The inlet concentration of tetraamminecopper(II) in the anolyte  $C_{[\text{Cu}(\text{NH}_3)_4]^{2+}}^{\text{increases}}$  to 0.13 mol L<sup>-1</sup>. Then, the tetraamminecopper(II) is regenerated, and its copper content becomes the new initial concentration of copper cations in the catholyte in the next discharging of the electrolyte set. The described process repeats until the inlet concentrations reach a cyclic steady-state around 0.2 mol L<sup>-1</sup>. Overall, the comparison of flow batteries at different operating conditions is only reasonable when comparing them at cyclic steady-state.

To assess the impacts of different operating conditions on the

To assess the impacts of different operating conditions on the flow battery's performance, we exemplarily investigate three operating conditions at cyclic steady-state. For this purpose, we independently double the electrical load  $R_{\rm TRFB}$  from 25 to 50  $\Omega$  and the cycle time  $t_{\rm cycle}$  from 1800 to 3600 s (Figure 8).

Increasing the electrical load  $R_{\rm TRFB}$  from 25 to 50  $\Omega$  decreases the averaged power density  $\overline{p}$  and averaged relative efficiency  $\overline{\eta}_{\rm th/Carnot}$  by about 50% (cf. Figure 8, orange bars). The averaged power density  $\overline{p}$  decreases because the current density decreases for larger electrical loads and, thus, the reaction rate decreases (cf. Equation (12)). As a result, the amount of reacted copper cations and, in turn, the averaged power density  $\overline{p}$  are almost halved. The amount of reacted copper cations also correlates to the working capacity of copper cations  $\Delta C_{\rm Cu^{2+}}^{\rm inlet}$  (cf. Figure 7c). The averaged relative efficiency  $\overline{\eta}_{\rm th/Carnot}$  decreases because the averaged power density decreases, but the number of regenerations cycles

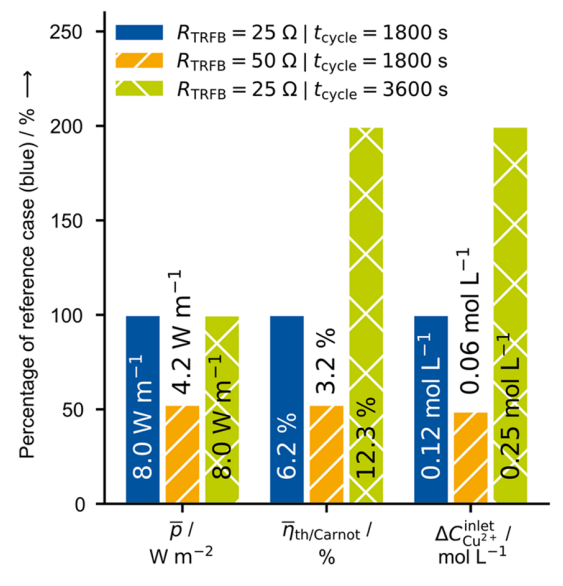


**Figure 8.** Time-averaged power density  $\bar{p}$ , time-averaged relative efficiency  $\bar{\eta}_{\text{th/Carnot}}$ , and working capacity of copper cations  $\Delta C_{\text{Cu}^{2+}}^{\text{inlet}}$  at cyclic steady-state for different operating conditions described by the electrical load  $R_{\text{TRFB}}$  and the cycle times  $t_{\text{cycle}}$ . Results are normalized by the reference operating conditions (blue).

Increasing the cycle time  $t_{\text{cycle}}$  from 1800 to 3600 s keeps the averaged power density  $\overline{p}$  nearly constant at 8 W m<sup>-2</sup> and almost doubles the averaged relative efficiency  $\bar{\eta}_{\text{th/Carnot}}$  to 12.3% (cf. Figure 8, red bars). The averaged power density  $\overline{p}$  remains nearly constant since it depends on the inlet concentration of copper cations in the catholyte: higher inlet concentrations lead to higher power densities and vice versa, which we discuss in more detail in Section 3.2. Although the battery is discharged deeper according to the working capacity of copper cations  $\Delta C_{C_1 2^{2+}}^{\text{inlet}}$ , the average inlet concentration of copper cations in the catholyte is still 0.2 mol L<sup>-1</sup> as long as the inlet concentration does not drop to zero within one discharging phase. Thus, the averaged power density  $\overline{p}$  remains nearly constant. The averaged relative efficiency  $\overline{\eta}_{th/Carnot}$  increases because the averaged power density  $\overline{p}$  remains nearly constant, but the number of regenerations is halved due to the doubled cycle time. Thus, the heat demand of the regeneration process is also halved, and, in turn, the average relative efficiency  $\overline{\eta}_{th/Carnot}$  almost doubles.

Overall, the averaged power density  $\bar{p}$  and averaged relative efficiency  $\bar{\eta}_{\text{th/Carnot}}$  depend on both the cycle time  $t_{\text{cycle}}$  and the electrical load  $R_{\text{TRFB}}$ . Although the cycle time  $t_{\text{cycle}}$  and electrical load  $R_{\text{TRFB}}$  show the same trends on the flow battery's performance (cf. Figure 8), they may have different impacts on the flow battery's performance when changed simultaneously or changed over a larger value range. Therefore, in the next section, we simultaneously vary the cycle time  $t_{\text{cycle}}$  and the electrical load  $R_{\text{TRFB}}$  to investigate the impact on the flow battery's performance at cyclic steady-state systematically.

## 3.2. Trade-Off Between Power Density and Efficiency

For the investigated Cu–NH<sub>3</sub> flow battery, an MPP exists at a specific current density i for each inlet concentration of copper cations in the catholyte (**Figure 9**a). The MPP decreases from 62 to 21 W m<sup>-2</sup> when lowering the inlet concentration of copper cations in the catholyte from 0.4 to 0.1 mol L<sup>-1</sup> (Figure 9a).

As the inlet concentration of copper cations decreases over one discharging phase due to the ongoing redox reaction (cf. Figure 7c), the MPP decreases over one discharging phase as well (cf. Figure 9a). [21] To maximize the averaged power density  $\overline{p}$ , we therefore track the MPP over one discharging phase similarly to photovoltaic systems [42] or fuel cells [39] (cf. Figure 9a). For this purpose, we adjust the current density i by altering the external load  $R_{\text{TRFB}}$  of the flow battery (cf. Figure 3a) during the entire discharging phase to realize the maximum power density at any point during the discharging phase.

However, at the MPP, kinetic losses (i.e., overpotentials) are significant<sup>[32]</sup> and decrease the averaged relative efficiency  $\overline{\eta}_{\text{th/Carnot}}$ . To maximize the averaged relative efficiency  $\overline{\eta}_{\text{th/Carnot}}$ , we move away from the MPP and also track fractions

21944296, 2022, 8, Downloaded

on Wiley Online Library for rules of use; OA articles are governed by the applicable Creative Commons

www.advancedsciencenews.com

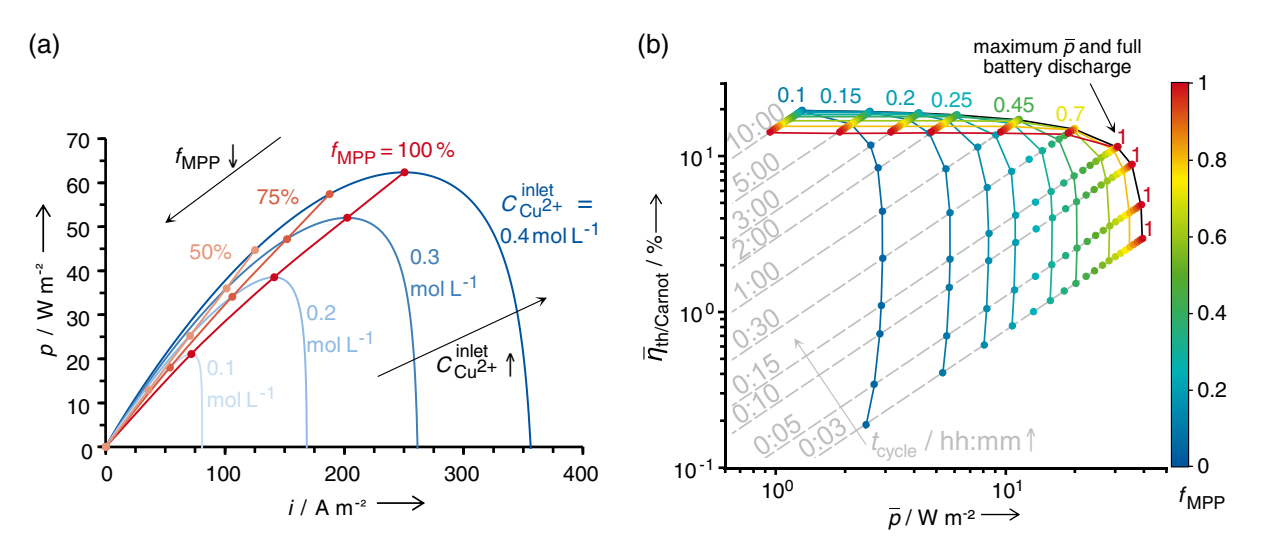


**Figure 9.** a) Power density p (blue lines) over current density i for different inlet concentrations of copper cations in the catholyte  $C_{\text{cu}^2}^{\text{clet}}$ . The red line connects the same fractions of the MPP, expressed by the maximum power point factor  $f_{\text{MPP}}$ . b) Averaged relative efficiency  $\overline{\eta}_{\text{th/Carnot}}$  over averaged power density  $\overline{p}$  for different cycle times  $t_{\text{cycle}}$  and maximum power point factors  $f_{\text{MPP}}$  for the regeneration process with an inlet temperature of 120 °C and heat transfer at a thermodynamic mean temperature of approximately 90 °C. Colored isolines connect constant maximum power point factors.

of the MPP expressed by the MPP factor  $f_{\text{MPP}}$ , which ranges from 0% to 100% (cf. Figure 9b).

Thereby, it is noticeable that the MPPs depend almost linearly on the current density for the various inlet concentrations (cf. Figure 9a, red line at  $f_{\rm MPP} = 100\%$ ). The same holds for the fractions of the MPP.

As already discussed, the current density *i* is proportional to the reaction rate (cf. Equation (12)), thus influencing the maximum cycle time until all copper cations in the catholyte are reduced to copper. Therefore, we vary the cycle time  $t_{cycle}$  and maximize both the average power density  $\bar{p}$  and average efficiency  $\overline{\eta}_{\text{th/Carnot}}$  (cf. Figure 9b). We obtain a Pareto frontier for each fraction of the MPP  $f_{\rm MPP}$  and derive an overall Pareto frontier (cf. Figure 9b, dashed black line). The highest average efficiency  $\overline{\eta}_{\text{th/Carnot}}$  is obtained for low fractions of the maximal power  $f_{\text{MPP}}$ . This anchor point of the Pareto frontier corresponds to a low average power density  $\overline{p}$  and a long cycle time  $t_{\text{cycle}}$ . The average power density  $\overline{p}$  increases and the average efficiency  $\overline{\eta}_{\text{th/Carnot}}$  decreases with increasing  $f_{\text{MPP}}$  and decreasing cycle times  $t_{\text{cycle}}$ . The optimal cycle time is always the time needed to discharge the flow battery completely. This optimal cycle time reduces with an increasing average power density  $\overline{p}$ . Once the optimal cycle time reduces to 15 min (cf. Figure 9b), the optimal fraction of the MPP reaches 100%, and the flow battery can still be discharged completely (i.e., break-even point). The average power density  $\overline{p}$  can be further increased by a shorter cycle time  $t_{
m cycle}.$  However, the average efficiency  $\overline{\eta}_{
m th/Carnot}$  reduces significantly since the cell can no longer be discharged completely. Consequently, it seems not preferable to have cycle times  $t_{\text{cycle}}$ that are shorter than the cycle time at which the battery is discharged entirely and at which the fraction of the MPP is 100%.

To compare the flow battery with the literature, we plot the technologies for power generation from low-temperature waste heat, discussed in more detail in Section 1 (cf. Figure 1), in Figure 10. Additionally, we plot the two following Pareto

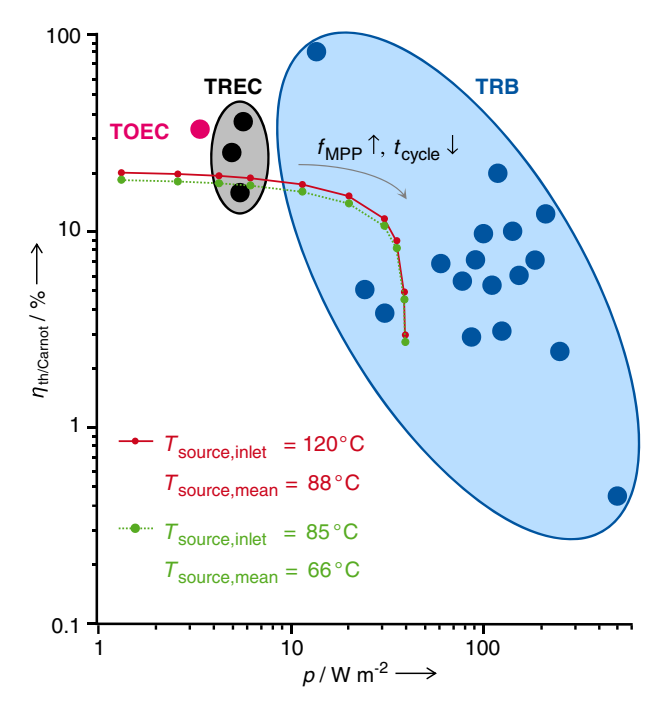


**Figure 10.** Relative efficiency  $\eta_{th/Carnot}$  over power density p for following technologies (redrawn and extended from Rahimi et al.<sup>[6]</sup>; further data taken from ref. [8–17]): TOEC, TREC, and TRB. For the investigated Cu–NH<sub>3</sub> flow battery, Pareto frontiers are shown for two regeneration processes using different heat source temperatures  $T_{\text{source,inlet}}$  also giving the corresponding thermodynamic mean temperatures  $T_{\text{source,mean}}$ . These Pareto frontiers of the flow battery depend on the operating mode of the discharging phase, described by the maximum power point factors  $f_{\text{MPP}}$  and the cycle time  $t_{\text{cycle}}$ .

frontiers for the  $Cu-NH_3$  flow battery: 1) regeneration process using a sensible heat source with an inlet temperature of 120 °C and heat transfer at a thermodynamic mean temperature of approximately 90 °C (solid red line); and 2) regeneration

21944296, 2022, 8, Downloaded from https://onlinelibrary.wiley.com/doi/10.1002/ente.202200152 by Forschungszentrum Jülich GmbH Research Center, Wiley Online Library on [13/11/2022]. See the Terms

ditions) on Wiley Online Library for rules of use; OA articles are governed by the applicable Creative Commons



process using a sensible heat source with an inlet temperature of 85 °C and heat transfer at a thermodynamic mean temperature of approximately 70 °C (dotted black line).

Figure 10 shows that both Pareto frontiers converge toward 38 W m<sup>-2</sup> for the maximum averaged power density  $\bar{p}$ . The maximum averaged power density  $\overline{p}$  is limited to 38 W m<sup>-2</sup> since the inlet concentration of copper cations in the catholyte fluctuates around  $0.2 \text{ mol L}^{-1}$ , at which the maximum power density p is 38 W m<sup>-2</sup> (cf. Figure 9a). However, higher averaged power densities  $\overline{p}$  might be possible for improved flow battery's settings using other electrolytes, operating temperatures, electrolyte velocities, cell geometries, electrodes, or bimetallic electrodes as indicated by the power densities reported for other flow batteries in the literature (cf. Figure 1). Another result shown in Figure 10 is that the Pareto frontier converges to a maximum averaged relative efficiency  $\overline{\eta}_{\text{th/Carnot}}$  of 18% for the regeneration process with an inlet temperature of 85 °C and 20% for the regeneration process with an inlet temperature of 120 °C. Thus, the selected regeneration process seems to slightly influence the averaged relative efficiency  $\overline{\eta}_{\text{th/Carnot}}$ .

## 3.3. Comparison of a Cu-NH3 Flow Battery with an ORC

The ORC can be considered as state-of-the-art technology to generate power from low-temperature waste heat, [3] thus it is frequently and comprehensively studied in the literature. [6] Therefore, we compare an ORC with the investigated Cu-NH<sub>3</sub> flow battery to 1) evaluate the potential of flow batteries as an alternative technology; and 2) estimate thresholds at which flow batteries become competitive. For the comparison, the ORC is fully optimized using the 1-stage CoMT-CAMD method presented by Schilling et al. [4] In the 1-stage CoMT-CAMD method, the ORC and its working fluid are simultaneously optimized to best exploit the potential of a given heat source. Thus, the 1-stage CoMT-CAMD method is an integrated design method leading to a fully optimized ORC.

The ORC is optimized for the identical conditions as the flow battery (cf. Section 2.2) to ensure a sound comparison: we use a sensible heat source with two inlet temperatures (i.e., 85 and 120 °C), a sensible heat sink with an inlet temperature of 15 °C, and a minimum pinch temperature of 2 K in all heat exchangers. The temperature increase of the heat sink is set to 3 K, and we use water, modeled as an ideal liquid with a constant heat capacity of  $4.18\,\mathrm{kJ\,kg^{-1}}$ , for the sensible heat source and sink. For the mass flow of the sensible heat source, we use  $10\,\mathrm{kg}\,\mathrm{s}^{-1}$  in accordance with a typical waste heat case study. [43] Hence, the sensible heat source (i.e., mass flow and inlet temperature) is identical for the ORC and the flow battery, but the cooling of the heat source depends on the efficiencies of the two technologies and, thus, may be different. Moreover, we limit the condensing pressure to the lowest pressure of the flow battery's regeneration processes: 1 bar for the regeneration process with an inlet temperature of 120 °C, and 0.275 bar for the regeneration process with an inlet temperature of 85 °C. As the objective function, we maximize the power production of the ORC because we assume waste heat as the energy input. Thus, the thermal efficiency is less relevant than the power production in this case.

To compare the results of the optimized ORC with the investigated Cu-NH<sub>3</sub> flow battery, we scale up the flow battery to the specified mass flow of the sensible heat source (i.e.,  $10 \text{ kg s}^{-1}$ ). We consider the three following discharge strategies of the flow battery: 1) discharge strategy that leads to the maximum averaged power density; 2) discharge strategy that leads to the break-even point; and 3) discharge strategy that leads to the maximum averaged relative efficiency. Using these discharge strategies, a sound comparison is possible between the ORC and flow battery: operating points are selected for the flow battery that maximize performance in its dynamic operation. The results of the comparison are summarized in Figure 11.

The power production of the flow battery increases from 15 to  $103\,kW$  for the heat source at  $120\,^{\circ}\text{C}$  and from 6 to  $42\,kW$  for the heat source at 85 °C, when changing the discharge strategy from the maximum averaged power density to the maximum averaged relative efficiency (cf. Figure 11). Simultaneously, the system size of the flow battery increases by a factor of 200. As expected, the power production is highest for the discharge strategy leading to

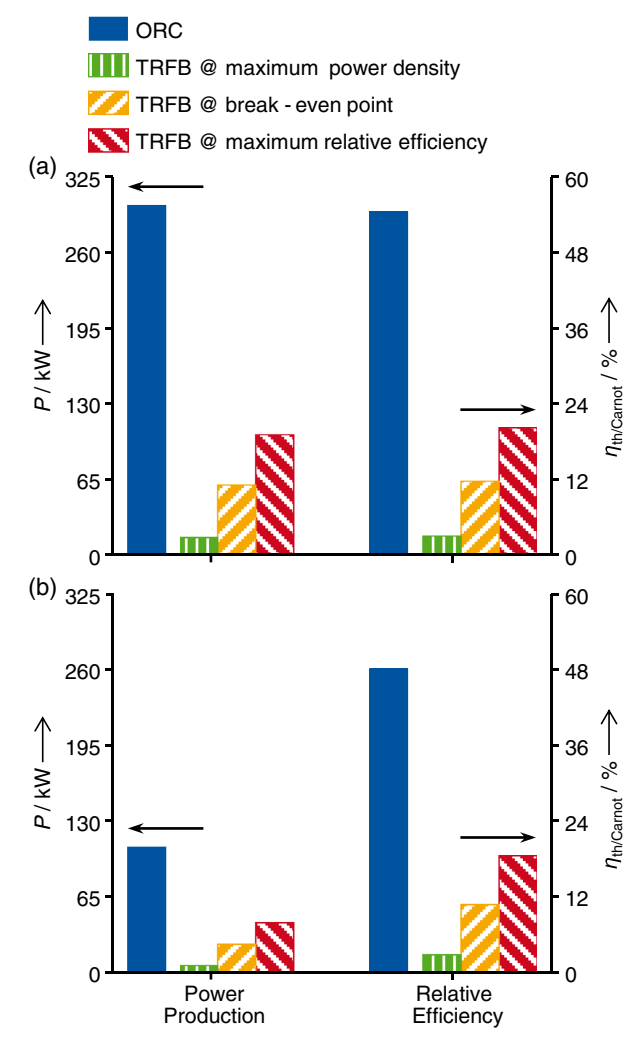


Figure 11. Comparison of a Cu-NH3 flow battery (TRFB) with a fully optimized organic Rankine cycle (ORC) for sensible heat source with an inlet temperature of a) 120 °C and b) 85 °C.

21944296, 2022, 8, Downloaded from https://onlinelibrary.wiley.com/doi/10.1002/ente.202200152 by Forschungszentrum Jülich GmbH Research Center, Wiley Online Library on [13/11/2022]. See the Terms and Conditions (https://onlinelibrary.wiley.com/doi/10.1002/ente.202200152 by Forschungszentrum Jülich GmbH Research Center, Wiley Online Library on [13/11/2022]. See the Terms and Conditions (https://onlinelibrary.wiley.com/doi/10.1002/ente.202200152 by Forschungszentrum Jülich GmbH Research Center, Wiley Online Library on [13/11/2022]. See the Terms and Conditions (https://onlinelibrary.wiley.com/doi/10.1002/ente.202200152 by Forschungszentrum Jülich GmbH Research Center, Wiley Online Library on [13/11/2022]. See the Terms and Conditions (https://onlinelibrary.wiley.com/doi/10.1002/ente.202200152 by Forschungszentrum Jülich GmbH Research Center, Wiley Online Library on [13/11/2022]. See the Terms and Conditions (https://onlinelibrary.wiley.com/doi/10.1002/ente.202200152 by Forschungszentrum Jülich GmbH Research Center, Wiley Online Library on [13/11/2022]. See the Terms and Conditions (https://onlinelibrary.wiley.com/doi/10.1002/ente.202200152 by Forschungszentrum Jülich GmbH Research Center, Wiley Online Library on [13/11/2022]. See the Terms and Conditions (https://onlinelibrary.wiley.com/doi/10.1002/ente.202200152 by Forschungszentrum Julich GmbH Research Center, Wiley Online Library.

and-conditions) on Wiley Online Library for rules of use; OA articles are governed by the applicable Creative Commons License

the maximum averaged relative efficiency because kinetic losses are minimal for this discharge strategy. Since the system size is difficult to compare between a flow battery and an ORC, we compare the power production of the ORC and the flow battery at the discharging strategy leading to the highest power production (i.e., bars with a red fill pattern, Figure 11). The ORC has a power production of 300 kW for the heat source at 120 °C and 107 kW for the heat source at 85 °C (cf. Figure 11). Thus, the ORC clearly exceeds the power production of the flow battery by 197 kW (+91%) for the heat source at 120 °C and by 65 kW (+55%) for the heat source at 85 °C. The difference becomes smaller for lower heat source temperatures.

However, the comparison is biased in favor of the ORC in several aspects: the ORC is fully optimized while the flow battery still has the potential for optimization. The optimization potential can be derived from the performances reported for thermally regenerative batteries (cf. Figure 1, Section 1): for example, further potential for optimization has been shown for the regeneration process, the electrolytes, the electrolyte velocities, the geometric cell design, or the operating conditions such as the operating temperature. In fact, the flow battery could become competitive with the ORC if relative efficiencies above 50% are achieved (cf. Figure 11). Such high relative efficiencies have already been reported in recent studies on bimetallic flow batteries (cf. Figure 1). Furthermore, the flow battery can also store energy, which will be important in future energy systems. In the flow battery is more flexible than an ORC.

Overall, the previous analysis suggests that the flow battery may only be an alternative technology to ORCs for power production and energy storage from low-temperature heat after optimizing its design, operating conditions, and regeneration process.

# 4. Conclusions

TRFBs have been recently proposed to produce power from industrial low-temperature waste heat. In this work, we perform a detailed numerical analysis of a Cu–NH<sub>3</sub> TRFB using a sensible heat source for regeneration with inlet temperatures of 85 and 120 °C. For this purpose, we developed a dynamic, open-access, full-cycle model of the Cu–NH<sub>3</sub> TRFB in Modelica. The full-cycle model is validated with experimental data taken from the literature, showing ARDs below 4%. From our analysis, two main conclusions can be drawn.

First, a dynamic full-cycle analysis of the Cu–NH<sub>3</sub> TRFB reveals the trade-off between power density and relative efficiency. This trade-off only depends on the strategy of the discharging phase and results in a Pareto frontier: the maximum averaged power density is 38 W m<sup>-2</sup> for both regeneration temperatures, whereas the maximum averaged relative efficiency is 20% at 120 °C and 18% at 85 °C. When adjusting the flow battery's operating point throughout the entire discharge cycle to realize the maximum power density at each time, 58% of the maximum averaged relative efficiency is achieved and 78% of the maximum averaged power density. Thus, the selected operating points are crucial for evaluating TRFBs, and the proposed discharge strategy enables the systematic selection of operating points for a holistic evaluation.

Second, a comparison of the Cu–NH<sub>3</sub> TRFB with a fully optimized ORC shows that the TRFB can reach 39% of power production of the optimal ORC for a sensible heat source with an inlet temperature of 85 °C and 34% for an inlet temperature of 120 °C. However, the flow battery still has the potential for further optimization, which needs to be exploited. Particularly for relative efficiencies above 50%, which have already been reported for other TRFBs (cf. Section 1), the TRFB could become competitive. In addition, the flow battery offers to store energy in contrast to the ORC, which could be advantageous in some applications in future energy system.

Overall, the Cu-NH<sub>3</sub> TRFB may be an alternative technology to the ORC to produce and store electrical power from low-temperature heat after further optimizing its regeneration process, electrolytes, operating conditions, and the design of the electrochemical cell.

# **Supporting Information**

Supporting Information is available from the Wiley Online Library or from the author.

# Acknowledgements

Simulations were performed with computing resources granted by RWTH Aachen University under project thes0456.

Open Access funding enabled and organized by Projekt DEAL.

# Conflict of Interest

The authors declare no conflict of interest.

# **Data Availability Statement**

The data that support the findings of this study are available in the supplementary material of this article.

# **Keywords**

dynamic simulations, electrochemical power production, heat to power, low-grade heat

Received: February 14, 2022 Revised: May 5, 2022 Published online: June 22, 2022

- [1] C. Forman, I. K. Muritala, R. Pardemann, B. Meyer, Renewable Sustainable Energy Rev. 2016, 57, 1568.
- [2] a) H. Jouhara, N. Khordehgah, S. Almahmoud, B. Delpech,
  A. Chauhan, S. A. Tassou, *Therm. Sci. Eng. Prog.* 2018, 6, 268; b)
  S. Brückner, S. Liu, L. Miró, M. Radspieler, L. F. Cabeza,
  E. Lävemann, *Appl. Energy* 2015, 151, 157.
- [3] P. Colonna, E. Casati, C. Trapp, T. Mathijssen, J. Larjola, T. Turunen-Saaresti, A. Uusitalo, J. Eng. Gas Turbines Power 2015, 137, 2157.
- [4] J. Schilling, D. Tillmanns, M. Lampe, M. Hopp, J. Gross, A. Bardow, Mol. Syst. Des. Eng. 2017, 2, 301.
- [5] J. Bao, L. Zhao, Renewable Sustainable Energy Rev. 2013, 24, 325.

21944296, 2022, 8, Downloaded from https://onlinelibrary.wiley.com/doi/10.1002/ente.202200152 by Forschungszentrum

Jülich GmbH Research Center, Wiley Online Library on [13/11/2022]. See the Terms

governed by the applicable Creative Commons



- [6] M. Rahimi, A. P. Straub, F. Zhang, X. Zhu, M. Elimelech, C. A. Gorski, B. E. Logan, Energy Environ. Sci. 2018, 11, 276.
- [7] D. Brogioli, F. La Mantia, Energy Environ. Sci. 2021, 14, 1057.
- [8] F. Zhang, J. Liu, W. Yang, B. E. Logan, Energy Environ. Sci. 2015, 8. 343.
- [9] F. Zhang, N. LaBarge, W. Yang, J. Liu, B. E. Logan, ChemSusChem **2015**, 8, 1043.
- [10] X. Zhu, M. Rahimi, C. A. Gorski, B. Logan, ChemSusChem 2016, 9. 873.
- [11] M. Rahimi, A. D'Angelo, C. A. Gorski, O. Scialdone, B. E. Logan, I. Power Sources 2017, 351, 45.
- [12] M. Rahimi, L. Zhu, K. L. Kowalski, X. Zhu, C. A. Gorski, M. A. Hickner, B. E. Logan, J. Power Sources 2017, 342, 956.
- [13] M. Rahimi, T. Kim, C. A. Gorski, B. E. Logan, J. Power Sources 2018, 373, 95.
- [14] S. Maye, H. Girault, P. Peljo, Energy Environ. Sci. 2020, 7, 2191.
- [15] W. Wang, H. Tian, G. Shu, D. Huo, F. Zhang, X. Zhu, J. Mater. Chem. A 2018, 11, 5991.
- [16] W. Wang, H. Tian, D. Huo, S. Yang, S. Li, X. Zhu, G. Shu, J. Power Sources 2021, 499, 229943.
- [17] Y. Shi, L. Zhang, Y. Zhang, J. Li, Q. Fu, X. Zhu, Q. Liao, Chem. Eng. J. **2021**, *423*, 130339.
- [18] D. S. Aaron, Q. Liu, Z. Tang, G. M. Grim, A. B. Papandrew, A. Turhan, T. A. Zawodzinski, M. M. Mench, J. Power Sources **2012**, *206*, 450.
- [19] P. Peljo, D. Lloyd, N. Doan, M. Majaneva, K. Kontturi, Phys. Chem. Chem. Phys. 2014, 16, 2831.
- [20] R. Springer, N. R. Cross, S. N. Lvov, B. E. Logan, C. A. Gorski, D. M. Hall, J. Electrochem. Soc. 2021, 168, 70523.
- [21] W. Wang, G. Shu, H. Tian, X. Zhu, J. Power Sources 2018, 388, 32.
- [22] H. Tian, W. Jiang, G. Shu, W. Wang, D. Huo, M. Z. Shakir, J. Electrochem. Soc. 2019, 166, A2814.
- [23] N. R. Cross, D. M. Hall, S. N. Lvov, B. E. Logan, M. J. Rau, Electrochim. Acta 2021, 388, 138527.
- [24] L. Zhang, Y. Li, X. Zhu, J. Li, Q. Fu, Q. Liao, Z. Wei, Ind. Eng. Chem. Res. 2019, 58, 7408.
- [25] Y. Zhang, L. Zhang, J. Li, X. Zhu, Q. Fu, Q. Liao, Y. Shi, Electrochim. Acta 2020, 331, 135442.
- [26] Z. Lu, Y. Zhang, L. Zhang, J. Li, Q. Fu, X. Zhu, Q. Liao, Sci. China Technol. Sci. 2021, 64, 696.

- [27] a) P. Chen, Y. Shi, L. Zhang, J. Li, X. Zhu, Q. Fu, Q. Liao, Ind. Eng. Chem. Res. 2020, 59, 21286; b) Y. Shi, L. Zhang, J. Li, Q. Fu, X. Zhu, Q. Liao, Y. Zhang, J. Power Sources 2020, 473, 228525.
- [28] F. Vicari, A. D'Angelo, Y. Kouko, A. Loffredi, A. Galia, O. Scialdone, J. Appl. Electrochem. 2018, 48, 1381.
- [29] P. Fritzson, Principles of Object Oriented Modeling and Simulation with Modelica 3.3. A Cyber-Physical Approach, 2nd ed., Wiley, Hoboken, NJ 2014.
- [30] A. A. Kulikovsky, Analytical Modeling of Fuel Cells, 2nd ed., Elsevier, Amsterdam 2019.
- [31] W. Schmickler, E. Santos, Interfacial Electrochemistry, 2nd ed., Springer, Berlin, Heidelberg 2010.
- [32] Springer Handbook of Electrochemical Energy, 1st ed. (Eds: C. Breitkopf, K. Swider-Lyons), Springer, Berlin, Heidelberg 2017.
- [33] V. M. Schmidt, Elektrochemische Verfahrenstechnik. Grundlagen, Reaktionstechnik, Prozessoptimierung, Wiley-VCH, Weinheim, 2003 (in German).
- [34] A. Hofmann, Physical Chemistry Essentials, 1st ed., Springer, Cham, Basel 2018.
- [35] CRC Handbook of Chemistry And Physics. A Ready-Reference Book Of Chemical And Physical Data, 99th ed. (Eds: J. R. Rumble, D. R. Lide, T. J. Bruno), CRC Press, Boca Raton 2018.
- [36] Aspen Technology, Inc., https://www.aspentech.com/en/products/ engineering/aspen-plus (accessed: January 2022).
- [37] E. W. Lemmon, I. H. Bell, M. L. Huber, M. O. McLinden, Reference Fluid Thermodynamic and Transport Properties-REFPROP, Version 10.0, NIST Standard Reference Database 23, National Institute of Standards and Technology, Gaithersburg 2018.
- [38] R. Tillner-Roth, D. G. Friend, J. Phys. Chem. Ref. Data 1998, 27, 63.
- [39] S. Ahmadi, S. Abdi, M. Kakavand, Int. J. Hydrogen Energy 2017, 42, 20430.
- [40] I. I. Clifford, E. Hunter, J. Phys. Chem. 2002, 37, 101.
- [41] J. A. Dean, N. A. Lange, Lange's Handbook of Chemistry, 15th ed., McGraw-Hill, NY 1999.
- [42] B. W. Williams, A. A. Helal, M. A. Elsaharty, A. K. Abdelsalam, N. E. Zakzouk, IET Renewable Power Gener. 2016, 10, 561.
- [43] F. Heberle, D. Brüggemann, Energies 2016, 9, 226.
- [44] M. Sterner, I. Stadler, Energiespeicher Bedarf, Technologien, Integration, 1st ed., Springer Vieweg, Berlin, Heidelberg, 2017 (in German).